

PLANETARY SCIENCE

Surface waves and crustal structure on Mars

D. Kim^{1,3*}, W. B. Banerdt², S. Ceylan¹, D. Giardini¹, V. Lekić³, P. Lognonné⁴, C. Beghein⁵, É. Beucler⁶, S. Carrasco⁷, C. Charalambous⁸, J. Clinton⁹, M. Drilleau¹⁰, C. Durán¹, M. Golombek², R. Joshi¹¹, A. Khan^{1,12}, B. Knapmeyer-Endrun⁷, J. Li⁵, R. Maguire¹³, W. T. Pike⁷, H. Samuel⁴, M. Schimmel¹⁴, N. C. Schmerr³, S. C. Stähler¹, E. Stutzmann⁴, M. Wieczorek¹⁵, Z. Xu⁴, A. Batov¹⁶, E. Bozdag¹⁷, N. Dahmen¹, P. Davis⁵, T. Gudkova¹⁶, A. Horleston¹⁸, Q. Huang¹⁷, T. Kawamura⁴, S. D. King¹⁹, S. M. McLennan²⁰, F. Nimmo²¹, M. Plasman⁴, A. C. Plesa²², I. E. Stepanova¹⁶, E. Weidner⁵, G. Zenhäusern¹, I. J. Daubar²³, B. Fernando²⁴, R. F. Garcia¹⁰, L. V. Posiolova²⁵, M. P. Panning²

We detected surface waves from two meteorite impacts on Mars. By measuring group velocity dispersion along the impact-lander path, we obtained a direct constraint on crustal structure away from the InSight lander. The crust north of the equatorial dichotomy had a shear wave velocity of approximately 3.2 kilometers per second in the 5- to 30-kilometer depth range, with little depth variation. This implies a higher crustal density than inferred beneath the lander, suggesting either compositional differences or reduced porosity in the volcanic areas traversed by the surface waves. The lower velocities and the crustal layering observed beneath the landing site down to a 10-kilometer depth are not a global feature. Structural variations revealed by surface waves hold implications for models of the formation and thickness of the martian crust.

The martian crust exhibits substantial variations in topography, inferred thickness, age, cratering, resurfacing, and volcanism (1). Constraining the variation of the crust's properties and composition with depth is crucial for understanding its origin and evolution (2). Inferences of crustal thickness and density variations, which are derived from joint analysis of topography and gravity data, suffer from substantial trade-offs (3). For example, the ~5-km topographic difference between the highly cratered southern highlands and the low-lying, less-cratered northern plains can be explained by differences in crustal thickness, by large variations in crustal density (4), or by a combination thereof.

The InSight mission to Mars (5) has provided direct constraints on the layering of the crust at the landing site (6). Analyses of body wave conversions and ambient noise wave field have constrained the crustal thickness beneath the InSight lander in Elysium Planitia as being 39 ± 8 km (7–9), providing a key anchoring point for global models of crustal thickness and density variations. Looking deeper, travel times of body waves from several marsquakes have enabled the determination of seismic velocity profiles of the upper mantle (10), core radius (8, 11), and mean density (12). Despite these achievements, the competing

effects of epicentral distance, source depth, and radial structure on body wave travel times (13) have stymied efforts to constrain lateral variations in structure using a single seismometer on Mars.

The velocity of surface waves, unlike that of body waves, depends on frequency, with lower-frequency waves sensitive to greater depths. The measurement of surface wave dispersion therefore provides a direct observation of the depth-dependent variation of seismic velocities averaged along the path from source to receiver (14). Until now, surface waves had not been observed on any marsquake records. Their absence could be due to the relatively small magnitude of the recorded seismic events (15), large source depths (8), and/or contamination of seismic data by long-period wind noise and atmospheric pressure waves (16). Strong crustal scattering on Mars (6, 17) can also impede the propagation and affect the visibility of surface waves, as was the case on the Moon (18).

We report here the first detection of surface waves on Mars in the seismic waveforms of events S1094b and S1000a. S1094b, which occurred on 24 December 2021, is the fourth largest seismic event [moment magnitude (M_W^{Ma}) = 4.0 ± 0.2] and has one of the longest-duration seismic signals recorded to date by

InSight (19), with coda energy persisting for >135 min. On the basis of the differential travel time of the direct P- and S-wave arrivals and the measured P-wave polarization, the initial distance and back azimuth estimates provided by the Marsquake Service were $59.7 \pm 6^\circ$ and 40° (-9° , $+18^\circ$), corresponding to a source region in Amazonis Planitia ~3460 km northeast from InSight (Fig. 1). The Mars Reconnaissance Orbiter (MRO) images taken between 24 and 25 December 2021 revealed a large impact crater in Amazonis Planitia 3532 km away from the lander and consistent with the source location estimated for S1094b (20). With broad frequency content and M_W similar to those of S1094b, event S1000a has also been identified as atypical on the basis of its seismic characteristics (19), and it was recently associated with an impact crater near the Tharsis province ~7460 km away from the InSight lander (20). The ground-truth identification of the two events as impacts removes all uncertainties related to hypocentral depth.

We applied standard marsquake data-processing methodologies (19) to the S1094b waveform data. An unusually large-amplitude seismic arrival was observed 800 s after the P-wave in the S-wave coda in the vertical component spectrogram (Fig. 2). The arrival's frequency content was considerably lower than typical P- and S-wave arrivals in the low-frequency family marsquakes (8, 10). Narrow-band filter banks of the raw vertical component data showed dispersion in the 6- to 18-s period range (Fig. 2). Frequency-dependent polarization analysis confirmed that particle motion was strongly elliptically polarized in the vertical plane (fig. S1E). The systematic phase shift between the vertical and horizontal components suggests that the arrival had a predominantly retrograde particle motion and arrived from 51° due northeast, consistent with the polarization of the direct P-wave (fig. S6).

Taken together, these characteristics allow the positive identification of this phase as the minor-arc Rayleigh wave (R1). Although strong elliptical polarization has been previously observed in the 3- to 30-s period range of the ambient seismic noise recordings, they were strictly polarized in the horizontal plane (16) and correlated with daytime wind direction on Mars. Despite heavy late afternoon winds, a comodulation analysis of the potential wind

¹Institute of Geophysics, ETH Zürich, Zürich, Switzerland. ²Jet Propulsion Laboratory, California Institute of Technology, Pasadena, CA, USA. ³Department of Geology, University of Maryland, College Park, MD, USA. ⁴Université Paris Cité, Institut de physique du globe de Paris, CNRS, Paris, France. ⁵Department of Earth, Planetary and Space Sciences, University of California, Los Angeles, CA, USA. ⁶Nantes Université, Université Angers, Le Mans Université, CNRS, UMR 6112, Laboratoire de Planétologie et Géosciences, Nantes, France. ⁷Bensberg Observatory, University of Cologne, Bergisch Gladbach, Germany. ⁸Department of Electrical and Electronic Engineering, Imperial College London, London, UK. ⁹Swiss Seismological Service, ETH Zürich, Zürich, Switzerland. ¹⁰Institut Supérieur de l'Aéronautique et de l'Espace ISAE-SUPAERO, Toulouse, France. ¹¹Max Planck Institute for Solar System Research, Göttingen, Germany. ¹²Physik-Institut, University of Zürich, Zürich, Switzerland. ¹³Department of Geology, University of Illinois Urbana-Champaign, Champaign, IL, USA. ¹⁴Geosciences Barcelona, CSIC, Barcelona, Spain. ¹⁵Université Côte d'Azur, Observatoire de la Côte d'Azur, CNRS, Laboratoire Lagrange, Nice, France. ¹⁶Schmidt Institute of Physics of the Earth, Russian Academy of Sciences, Moscow, Russia. ¹⁷Department of Geophysics, Colorado School of Mines, Golden, CO, USA. ¹⁸School of Earth Sciences, University of Bristol, Bristol, UK. ¹⁹Department of Geosciences, Virginia Tech, Blacksburg, VA, USA. ²⁰Department of Geosciences, Stony Brook University, Stony Brook, NY, USA. ²¹Department of Earth and Planetary Sciences, University of California Santa Cruz, Santa Cruz, CA, USA. ²²Institute of Planetary Research, German Aerospace Center (DLR), Berlin, Germany. ²³Department of Earth, Environmental, and Planetary Sciences, Brown University, Providence, RI, USA. ²⁴Department of Earth Sciences, University of Oxford, Oxford, UK. ²⁵Malin Space Science Systems, San Diego, CA, USA.

*Corresponding author. Doyeon Kim (doyeon.kim@erdw.ethz.ch)

injection during the R1 arrival documented excess seismic energy over that generated by wind between 8 and 15 s at the time of the observation (fig. S3). Moreover, we confirmed that the seismic data recorded during the surface wave arrival were not contaminated by any known electromechanical artifacts associated with the seismic sensor or the InSight spacecraft system (21).

We found no evidence for Love waves in the S1094b records. This observation is consistent with an impact origin for S1094b, because an isotropic source would primarily excite Rayleigh waves. The detection of Rayleigh waves from this impact source, but not from other low-frequency marsquakes, supports the argument that the marsquakes recorded to date are generally too deep to effectively excite surface waves (22). Our waveform simulation confirms that surface waves from shallow seismic sources are far more likely to be detectable, given the diurnal ambient noise level on Mars (fig. S15).

We observed an additional anomalous seismic arrival ~75 min after the identified R1 (fig. S2). As for the R1 observation, the time of this arrival was far outside the time window for a potential direct or ground-coupled infrasound wave originating from the impact source region (20, 23). However, the timing was consistent with that expected for the major-arc Rayleigh wave (R2) that propagated in the opposite direction around Mars. Dispersion and enhanced elliptical polarization in the vertical plane in the 6- to 11-s period range supports the R2 interpretation. Although the frequency content of this arrival was comparable to that of R1, broadband environmental injection in the analysis window was also evident (fig. S4). Because of the low signal-to-noise ratio, the direction of propagation and particle motion of this phase were unclear, and thus the identification of R2 is not definitive. We found no evidence for the arrival of surface wave overtones or multi-orbiting Rayleigh waves in the S1094b waveforms (19).

Surface wave data on Earth are typically interpreted assuming that propagation occurs along the great circle path from source to receiver and that it can be related to the average flat-layer structure along that path (24). Using a number of crustal thickness models constructed on the basis of gravimetric data and the extrapolated crustal thickness estimates from the InSight location (25), our kinematic ray tracing predicted negligible deviations from great circle paths for R1 and R2 that were <0.2% of the total travel time (19). We measured the group velocities of R1 and R2 and obtained average values of 2.77 and 3.14 km/s, respectively, which implies structural differences along their propagation paths (fig. S7). Indeed, whereas the R1 path traverses only the northern lowlands, a large fraction of the R2 path crosses

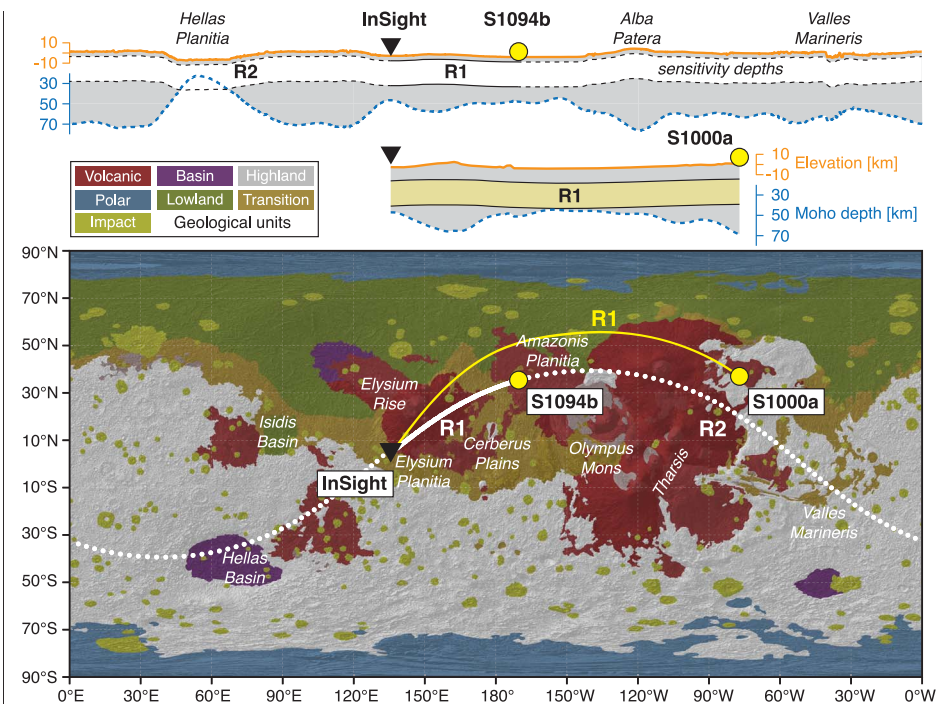


Fig. 1. Locations of two large meteorite impacts (yellow circles) identified in MRO images. The great circle paths for S1094b R1 (solid) and R2 (dashed) are shown in white, and the R1 path for S1000a is shown in yellow. Background topographic relief is from the Mars Orbiter Laser Altimeter (47). The distribution and sequence of major geological unit groups of Hesperian and Amazonian age (32) are overlaid. Global elevation (orange) and the crust-mantle boundary depth profiles (25) along the R1 and R2 paths (dashed blue) are shown at the top.

the southern highlands, and between 12 and 17% of the path passes through the Hellas impact basin, where the crust has been largely removed and replaced by uplifted mantle (26). Therefore, the crustal thickness within the Hellas impact basin could be as low as a few kilometers (25), and R2 would travel at a seismic velocity of the uppermost mantle (corresponding to S-wave velocities, $V_S = 4$ to 4.5 km/s) at periods of 10 to 16 s. The observed higher value in the average group velocity of R2 with respect to R1 could then be accounted for by Hellas alone, and as a result the average crustal velocity of the southern and northern hemispheres would be very similar (fig. S19).

Both phases showed little dispersion in the observed frequency range, which is primarily sensitive to crustal structure between ~5- and 30-km depth (Fig. 2C). Path-averaged radial P- and S-wave velocity profiles were inverted using the R1 measurements with multiple approaches (Fig. 2C, and figs. S9 to S11), and regardless of the parameterization strategies considered (19), we obtained a uniform V_S of ~3.2 km/s, with a slight linear increase down to a 30-km depth. At greater depths, we lose sensitivity because of the lack of dispersion measurements at long periods (Fig. 2). At the shallowest depths, we cannot rule out a thin slow layer;

however, because of the nonlinear relationship between V_S profiles and surface wave sensitivity kernels (Fig. 2C), the greatest permissible thickness of such a layer depends on its V_S . The uniform V_S in the 5- to 30-km crustal depth range is different from the three-layer crustal structure observed beneath InSight (7–9). The obtained V_S was substantially higher in the upper 10 km and was similar to the average velocities of the second and third layers beneath the lander (Fig. 2D), but did not show the same velocity jump around the 20-km depth. From the comparison of the local and the R1 path-average velocity structures, we concluded that the low V_S observed down to the 8- to 10-km depth below the lander was a local feature, and if it is present in other parts along the path, it must be restricted to only few kilometers below the surface. We cannot exclude the presence of deeper layering in the crust, but this would have to occur at varying depths along the path to be averaged in the observed linear V_S increase with depth.

The high crustal seismic velocities inferred from the S1094b dispersion analysis were supported by S1000a data. Two distinct long-period arrivals, at the ~20-s and ~30-s periods, were visible in the vertical component spectrogram of S1000a in the R1 group arrival time

Fig. 2. Seismic waveforms and velocity profiles.

(A) Vertical component seismogram of S1094b band-pass filtered between 1 and 5 s (gray) and between 8 and 15 s (blue) with P- and S-wave picks (black vertical lines). Narrow-band filter banks and envelopes show dispersed signals 800 s after the P-wave. **(B)** Vertical component S-transform showing a large-amplitude seismic arrival that exhibits dispersion [compare with (A)]. The frequency domain envelope averaged across the 8- to 15-s period range is plotted at the top of the spectrogram. Other characteristics enabling the identification of this dispersive arrival as R1 are described in the supplementary materials (19). **(C)** Depth sensitivity kernels and data misfit of R1 in S1094b (inset). The mean and SD are drawn from 10 pairs of dispersion measurements (fig. S7). Kernels in dashed lines were computed on the basis of the three-layer crustal model in (7) denoted as KE2021. Note the substantial differences between the kernels caused by the different velocity profiles. Shaded kernels and predictions are computed using the average model in (D). **(D)** Posterior distribution of V_s structure inverted from the group velocity measurements of S1094b R1 (K1094bR1). Posterior distribution and prediction are based on the best-fitting 10,000 models after one million iterations. Depths where sensitivity is inadequate (<40% in cumulative kernel strength) are muted. The range of V_s in the three-layer crustal models beneath the lander (7) are indicated by gray dashed lines. **(E)** Posterior distribution of the V_s structure inverted with the group velocity measurements of the S1000a R1 (K1000aR1) at ~20-s and ~30-s periods (fig. S13). Blue and yellow horizontal error bars denote the interquartile ranges of the posterior distributions in (D) and (E), respectively.

are computed using the average model in (D). **(D)** Posterior distribution of V_s structure inverted from the group velocity measurements of S1094b R1 (K1094bR1). Posterior distribution and prediction are based on the best-fitting 10,000 models after one million iterations. Depths where sensitivity is inadequate (<40% in cumulative kernel strength) are muted. The range of V_s in the three-layer crustal models beneath the lander (7) are indicated by gray dashed lines. **(E)** Posterior distribution of the V_s structure inverted with the group velocity measurements of the S1000a R1 (K1000aR1) at ~20-s and ~30-s periods (fig. S13). Blue and yellow horizontal error bars denote the interquartile ranges of the posterior distributions in (D) and (E), respectively.

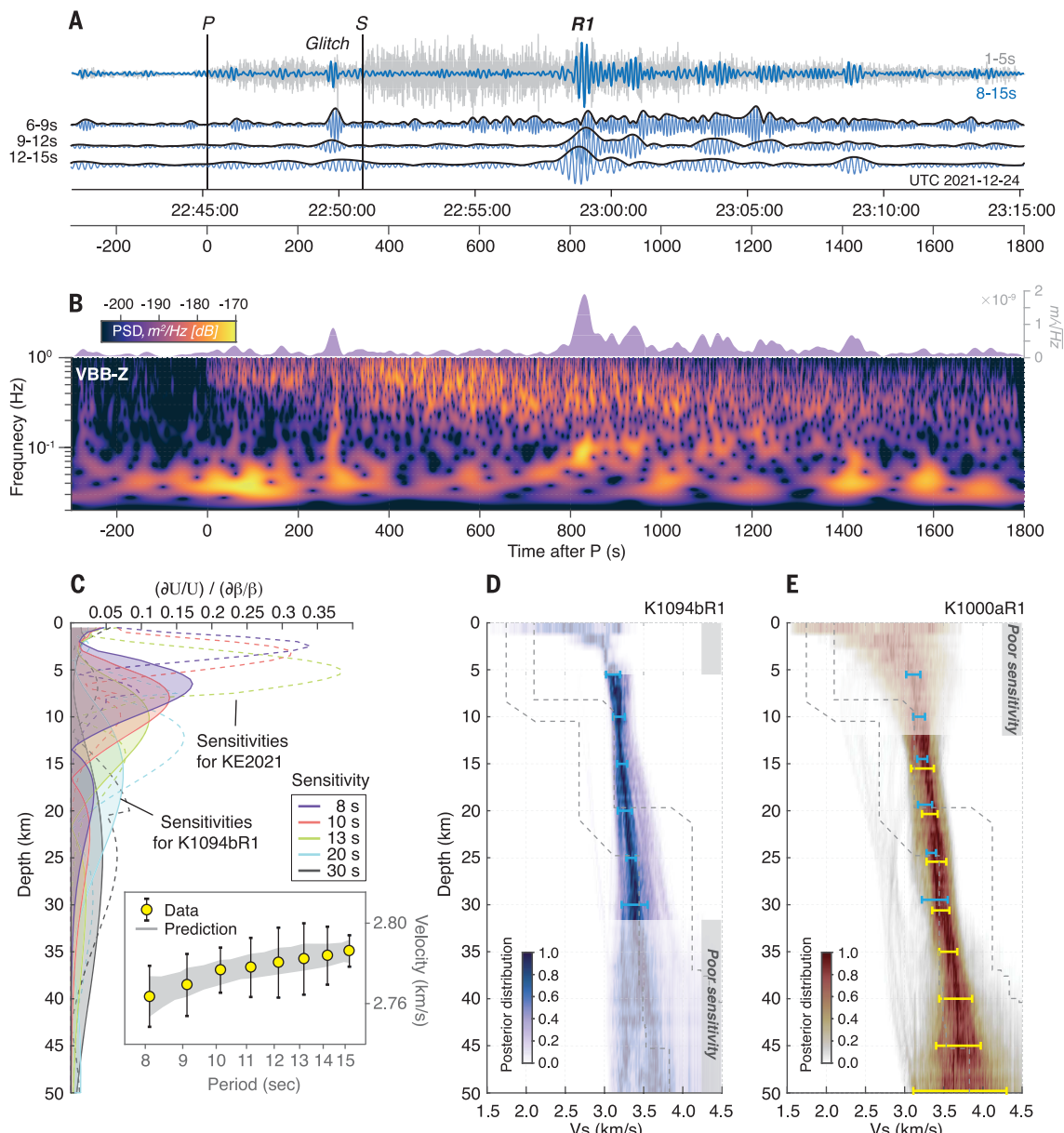
range predicted on the basis of the posterior distribution of V_s (fig. S12). Although R1 in S1094b showed clear polarization, the comparative strength of the environmental injection during the expected R1 window of S1000a prevents a definitive identification. The inferred V_s structure using the S1000a group velocity measurements at the ~20-s and ~30-s periods (2.73 and 2.83 km/s, respectively) overlaps with our posterior V_s distribution for S1094b down to 30-km depth, and provides additional constraints to image a slowly increasing V_s in the lower crust down to 45-km depth (Fig. 2E).

This agreement suggests a high degree of similarity in the average crustal structure along the two R1 paths.

Unlike dispersion, the frequency dependence of Rayleigh wave ellipticity, expressed as the ratio of horizontal-to-vertical amplitude (H/V), is strongly sensitive to the structure directly beneath InSight. We found that the H/V measurements made on R1 were consistent with previous models of crustal layering beneath the lander (figs. S16 and S17), as were P- to S-wave conversions in the P-wave coda of S1094b, which showed prominent arrivals at

2.4, 4.8, and 7.2 s after the direct P arrival (figs. S20 and S21). Even with a single event, we can confirm that the shallow crustal structure at the landing site down to 10-km depth was substantially slower than the average crustal velocity sampled by the R1 path.

The observed surface waves allowed us to expand the current understanding of crustal structure on Mars beyond the crustal layering inferred beneath the InSight landing site (7). We found that the low V_s layer extending down to 10-km depth in the shallow crust of Elysium Planitia does not exist globally on



Mars. Instead, the average crustal velocities along the R1 paths of S1000a and S1094b (Fig. 3) were considerably faster and are likely to be more representative of the average crustal structure. Large geographic variations in upper crustal structure hold implications for interpreting waveforms of surface-bouncing seismic waves such as PP and SS and must be explicitly accounted for when constructing models of the spherically symmetrical structure of Mars. These structural variations hold clues for the deeper signature of surface geologic units and for interpretations of gravity data.

A large portion of the R1 paths between Elysium and Amazonis Planitia passes through the Elysium rise, the largest volcanic province in the northern lowlands (Fig. 1). Its surface geology is characterized by lava flows of Hesperian to Amazonian age, reaching up to several kilometers of thickness and representing a history of major resurfacing (27). Beyond Elysium, the S1000a R1 path again encounters extensive regions covered by Hesperian and Amazonian volcanics in Amazonis Planitia and north of Alba Patera. By contrast, the plains around the InSight lander are composed of Early Hesperian and Early Amazonian lava flows (28, 29), and their limited thickness is insufficient to affect R1 dispersion. Below ~200 m, weaker sedimentary material is suggested to extend in places at least to 5- to 6-km depth on the basis of the phyllosilicate signatures and layered sedimentary rocks brought up in the central peaks of large impact craters (30).

Similar constraints are provided by density inferred from gravity data. The maximum permissible density of the overall crust on Mars (2850 to 3100 kg/m 3) is lower than the density of most martian basaltic materials found at the surface, as estimated by gamma-ray compositional mapping (31) and by mineralogical norms for SNC meteorites of predominantly Amazonian age [see summary in (25)]. The two factors contributing to a layered crustal density structure on a global scale could be of a less mafic (less dense) composition and/or an elevated porosity (6, 7, 25) (Fig. 3).

Most of the R1 paths pass through regions resurfaced by relatively young volcanic rocks, and this results in similar, higher densities of the upper and lower crust. Although Elysium volcanic cumulates are only a few kilometers thick (32), and thus within the uppermost zone of poor seismic sensitivity (Fig. 2), their magmatic history influenced the nature of the whole crust in this region (33, 34). The average ratio of intrusive to extrusive magmatism on Mars (35, 36) implies that intrusives account for >5 km of average crustal thickness integrated over the entire Elysium rise and even more near the volcanic centers traversed by R1 (Fig. 1). One proposal for Mars is that intrusive rocks (i.e., magma chamber centers) would concentrate at greater depths than on Earth (33).

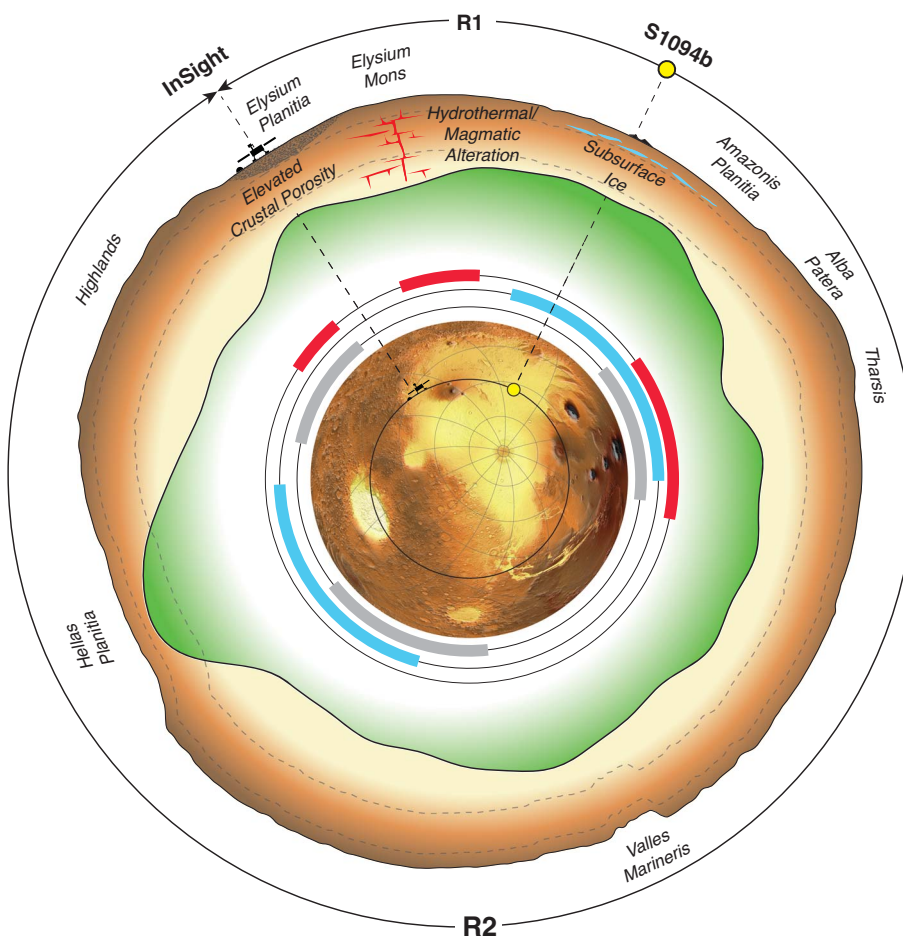


Fig. 3. Cross section of the S1094b surface wave path through Mars. Surface topography (47) and crustal thickness (25) with a 20× vertical exaggeration are shown along the path of R1 and R2, with major geological provinces labeled at the surface and potential subsurface structures that affect surface wave velocity. The approximate sampling depth of the observed surface waves is indicated by a gray dashed line. The inset context map shows the topography along the surface wave paths. The colored arcs indicate the path length(s) through provinces with surface volcanism (red), ice stability at latitudes >30° (cyan), and cratered highlands (gray).

These intrusive magmas represent, at least in part, residues of the partial melting giving rise to surface lavas, and thus they are likely of greater density (37) and have elevated seismic wave speeds closer to values typical of basaltic volcanic rocks, consistent with the path-average velocity profiles that we observed below a 5-km depth (Fig. 2).

Substantial porosity is also likely to be present in the upper crustal layers beneath the lander (6, 7, 25). Their low V_S is compatible with fractured basalt having, for example, 10% porosity, although the exact amount depends strongly on both the aspect ratio of the pore spaces and material contained therein (fig. S22). However, the higher path-averaged velocities that we observed in the upper 10 km would require lower porosity, which could result from viscous closure of pore spaces caused by the thermal annealing expected to accompany

volcanic resurfacing processes (25, 38), partial filling of pore spaces by the deposition of precipitated minerals from a briny ancient aquifer system (39), or the presence of a deep cryosphere or substantial water table beneath the thick Amazonian lava flows along the R1 path (19, 40, 41) (Fig. 3). Images from the High Resolution Imaging Science Experiment of the S1094b impact crater show large blocks of pure ice ejected from the shallower layers (20). This would not be expected to be the case near InSight, because the shallow crust with a V_S of 1.7 to 2.1 km/s in the upper 8 to 11 km (7) rules out an ice-saturated cryosphere (39).

Another possibility is that a low-density, high-porosity layer beneath InSight results from ejecta deposited by the Utopia impact (25). Because ejecta thickness is a strong function of radial distance, one would expect the ejecta

thickness averaged along the R1 path to be much less than that beneath InSight, which is consistent with observations.

Regardless of the exact origin, composition, and/or porosity, the variations of the martian crustal seismic structure presented here are likely correlated with density variations, because both temperature and compositional variations increase density together with V_s . Therefore, our results imply greater crustal densities between Elysium and Amazonis Planitia than directly beneath the lander. This result is consistent with previous estimates of higher crustal density beneath the Elysium rise of $3100 \pm 100 \text{ kg m}^{-3}$ (42) and lower density beneath the lander (43) from gravity topography measurements. Density variations would also affect inferences of crustal thickness from topographic and gravity signals associated with the crustal dichotomy (4, 25). Currently, both exogenic processes [i.e., one or more large impacts (44)] and endogenic processes [i.e., mantle convection (45)], or a combination thereof (46), continue to be debated as the origin of the dichotomy. Both processes would be expected to generate a basaltic secondary crust in the northern lowlands, consistent with the R1 observations from the two recent impacts. However, if confirmed by further analyses or other events, the S1094b R2 observation of similar group velocities across the southern hemisphere (once corrected for the path in the Hellas impact basin) preliminarily indicates that the crustal structure at relevant depths could be substantially similar north and south of the dichotomy (Fig. 3).

REFERENCES AND NOTES

1. S. R. Taylor, S. M. McLennan, *Planetary Crusts: Their Composition, Origin, and Evolution* (Cambridge Univ. Press, 2009).
2. S. E. Smrekar et al., *Space Sci. Rev.* **215**, 3 (2019).
3. M. T. Zuber, *Nature* **412**, 220–227 (2001).
4. V. Belleguic, P. Lognonné, M. Wieczorek, *J. Geophys. Res. Planets* **110**, E002437 (2005).
5. W. B. Banerdt et al., *Nat. Geosci.* **13**, 183–189 (2020).
6. P. Lognonné et al., *Nat. Geosci.* **13**, 213–220 (2020).
7. B. Knapmeyer-Endrun et al., *Science* **373**, 438–443 (2021).
8. C. Durán et al., *Phys. Earth Planet. Inter.* **325**, 106851 (2022).
9. D. Kim et al., *J. Geophys. Res. Planets* **126**, JE006983 (2021).
10. A. Khan et al., *Science* **373**, 434–438 (2021).
11. S. C. Stähler et al., *Science* **373**, 443–448 (2021).
12. A. Khan, P. A. Sossi, C. Liebske, A. Rivoldini, D. Giardini, *Earth Planet. Sci. Lett.* **578**, 117330 (2022).
13. A. Khan et al., *Phys. Earth Planet. Inter.* **258**, 28–42 (2016).
14. M. N. Toksöz, D. L. Anderson, *J. Geophys. Res.* **71**, 1649–1658 (1966).
15. M. Böse et al., *Bull. Seismol. Soc. Am.* **111**, 3003–3015 (2021).
16. É. Stutzmann et al., *J. Geophys. Res. Planets* **126**, e2020JE006545 (2021).
17. M. van Driel et al., *J. Geophys. Res. Planets* **126**, e2020JE006670 (2021).
18. A. M. Dainty et al., *Moon* **9**, 11–29 (1974).
19. Materials and methods are available as supplementary materials.
20. L. V. Posiolova et al., *Science* **378**, 412–417 (2022).
21. D. Kim et al., *Bull. Seismol. Soc. Am.* **111**, 2982–3002 (2021).
22. D. Giardini et al., *Nat. Geosci.* **13**, 205–212 (2020).
23. R. F. Garcia et al., *Nat. Geosci.* **15**, 774–780 (2022).
24. P. Moulik et al., *Geophys. J. Int.* **228**, 1808–1849 (2022).
25. M. A. Wieczorek et al., *J. Geophys. Res. Planets* **127**, e2022JE007298 (2022).
26. M. A. Wieczorek, R. J. Phillips, *Icarus* **139**, 246–259 (1999).
27. T. Platz, G. Michael, *Earth Planet. Sci. Lett.* **312**, 140–151 (2011).
28. M. Golombek et al., *Space Sci. Rev.* **214**, 84 (2018).
29. M. Golombek et al., *Nat. Commun.* **11**, 1014 (2020).
30. L. Pan et al., *Icarus* **338**, 113511 (2020).
31. D. Baratoux et al., *J. Geophys. Res. Planets* **119**, 1707–1727 (2014).
32. K. L. Tanaka, S. J. Robbins, C. M. Fortezzo, J. A. Skinner Jr., T. M. Hare, *Planet. Space Sci.* **95**, 11–24 (2014).
33. L. Wilson, J. W. Head III, *Rev. Geophys.* **32**, 221–263 (1994).
34. E. H. Christiansen, M. G. Best, J. Radabaugh, in *Planetary Volcanism Across the Solar System*, T. K. P. Gregg, R. M. C. Lopes, S. A. Fagents, Eds. (Elsevier, 2022); pp. 235–270.
35. G. J. Taylor, *Chem. Erde* **73**, 401–420 (2013).
36. B. A. Black, M. Manga, *J. Geophys. Res. Planets* **121**, 944–964 (2016).
37. F. M. McCubbin, H. Nekvasil, A. D. Harrington, S. M. Elardo, D. H. Lindsley, *J. Geophys. Res.* **113**, E11013 (2008).
38. S. Gyalay, F. Nimmo, A. C. Plesa, M. Wieczorek, *Geophys. Res. Lett.* **47**, e2020GL088653 (2020).
39. M. Manga, V. Wright, *Geophys. Res. Lett.* **48**, e2021GL093127 (2021).
40. S. M. Clifford et al., *J. Geophys. Res. Planets* **115**, E003462 (2010).
41. B. De Toffoli, M. Massironi, F. Mazzarini, A. Bistacchi, *J. Geophys. Res. Planets* **126**, e2021JE007007 (2021).
42. A. Broquet, M. A. Wieczorek, *J. Geophys. Res. Planets* **124**, 2054–2086 (2019).
43. T. V. Gudkova, I. E. Stepanova, A. V. Batov, *Sol. Syst. Res.* **54**, 15–19 (2020).
44. J. C. Andrews-Hanna, M. T. Zuber, W. B. Banerdt, *Nature* **453**, 1212–1215 (2008).
45. F. Nimmo, K. Tanaka, *Annu. Rev. Earth Planet. Sci.* **33**, 133–161 (2005).
46. R. I. Citron, M. Manga, D. J. Hemingway, *Nature* **555**, 643–646 (2018).
47. D. E. Smith et al., *Science* **284**, 1495–1503 (1999).
48. InSight Marsquake Service, “Mars Seismic Catalogue, InSight Mission; VII 2022-07-01” (ETHZ, IPGP, JPL, ICL, Univ. of Bristol, 2022); <https://doi.org/10.12686/a18>.
49. InSight Mars SEIS Data Service, “InSight SEIS Data Bundle” (PDS Geosciences, 2019); <https://doi.org/10.17189/1517570>.
50. InSight Mars SEIS Data Service, “SEIS raw data, Insight Mission (IPGP, JPL, CNES, ETHZ, ICL, MPS, ISAE-Supæro, LPG, MFSC, 2019); https://doi.org/10.18715/SEIS.INSIGHT.XB_2016.
51. P. Lognonné et al., *Space Sci. Rev.* **215**, 12 (2019).

ACKNOWLEDGMENTS

This paper is InSight contribution number 266. The authors acknowledge the National Aeronautics and Space Administration (NASA), Centre National d’Études Spatiales (CNES), their partner agencies and institutions (UKSA, SSO, DLR, JPL, IPGP-CNRN, ETHZ, IC, and MPS-MPG), and the flight operations team at JPL.

SISMOC, MSDS, IRIS-DMC, and PDS for providing the SEED SEIS data. We acknowledge the thorough and thoughtful reviews from the editor and from three anonymous reviewers that greatly improved the manuscript. **Funding:** D.K., S.C., D.G., J.C., C.D., A. K., S.C.S., N.D., and G.Z. were supported by the ETH+ funding scheme (ETH+02 19-1: “Planet Mars”). Marsquake Service operations at ETH Zürich were supported by ETH Research grant ETH-06 17-02. N.C.S. and V.L. were supported by NASA PSP grant no. 80NSSC18K1628. Q.H. and E.B. are funded by NASA grant 80NSSC18K1680. C.B. and J.L. were supported by NASA InSight PSP grant no. 80NSSC18K1679. S.D.K. was supported by NASA InSight PSP grant no. 80NSSC18K1623. P.L., E.B., M.D., H.S., E.S., M.W., Z.X., T.W., M.P., R.F.G. were supported by CNES and the Agence Nationale de la Recherche (ANR-19-CE31-0008-08 MAGIS) for SEIS operation and SEIS Science analysis. A.H., C.C. and W.T.P. were supported by the UKSA under grant nos. ST/R002096/1, ST/W002523/1 and ST/V00638X/1. Numerical computations of McMC Approach 2 were performed on the S-CAPAD/DANTE platform (IPGP, France) and using the HPC resources of IDRIS under the allocation A0110413017 made by GENCI. A.H. was supported by the UKSA under grant nos. ST/R002096/1 and ST/W002523/1. F.N. was supported by InSight PSP 80NSSC18K1627. I.J.D. was supported by NASA InSight PSP grant no. 80NSSC20K0971. L.V.P. was funded by NASA-NNI12AA01C with subcontract JPL-1515835. The research was carried out in part by W.B.B., M.G. and M.P.P. at the Jet Propulsion Laboratory, California Institute of Technology, under a contract with the National Aeronautics and Space Administration (80NM0018D0004). **Author contributions:** D.K., S.C., D.G., V.L., P.L., C.B., E.B., J.C., A.K., B.K., J.L., M.S., S.C.S., and E.S. analyzed the seismic data and contributed to the detection and identification of the surface wave arrivals. D.K., V.L., C.B., M.D., R.J., B.K., J.L., R.M., H.S., and E.W. performed the inversions. C.C. and W.T.P. performed the comodulation analysis. S.C.S. performed the analysis on ray tracing. D.K. performed waveform simulations. S.C., B.K., and Z.X. performed the H/V analysis. D.K., C.D., and B.K. performed the receiver function analysis. D.K., S.C., C.C., J.C., C.D., S.C.S., N.D., A.H., T.K., M.P., and G.Z. reviewed the continuous data and detected seismic events. D.K., W.B.B., S.C., D.G., V.L., P.L., C.B., J.C., M.G., A.K., B.K., J.L., R.M., N.S., S.C.S., M.S., E.S., M.W., E.B., P.D., Q.H., S.K., S.M.M., F.N., A.C.P., and R.F.G. contributed to the interpretation of the results. D.K. wrote the main paper with contribution from D.G. and V.L. D.K., W.B.B., S.C., V.L., C.B., J.C., M.G., A.K., B.K., J.L., W.T.P., R.M., N.S., S.C.S., M.S., E.S., M.W., E.B., P.D., Q.H., S.K., S.M.M., F.N., A.C.P., and R.F.G. edited the main text and supplementary materials. D.G., P.L., J.C., S.C.S., A.H., I.J.D., B.F., R.F.G., and L.V.P. performed S1094b and S1000a impact analysis and participated in discussions. W.B.B. and M.P.P. managed the InSight mission. P.L., D.G., W.T.P., and W.B.B. led the development of the SEIS instrument. **Competing interests:** The authors declare no competing interests. **Data and materials availability:** The InSight event catalog (48) and waveform data are available from the IRIS-DMC, NASA-PDS (49), and IPGP (50) data centers. Complete descriptions of the SEIS instrument and seismic channels are in (51). **License information:** Copyright © 2022 the authors, some rights reserved; exclusive licensee American Association for the Advancement of Science. No claim to original US government works. <https://www.science.org/about/science-licenses-journal-article-reuse>

SUPPLEMENTARY MATERIALS

science.org/doi/10.1126/science.abq7157

Materials and Methods

Supplementary Text

Figs. S1 to S22

References (52–91)

Submitted 28 April 2022; accepted 22 September 2022
10.1126/science.abq7157

Surface waves and crustal structure on Mars

D. Kim^W. B. Banerdt^S. Ceylan^D. Giardini^V. Lekić^P. Lognonné^C. Beghein^É. Beucler^S. Carrasco^C. Charalambous^J. Clinton^M. Drilleau^C. Durán^M. Golombek^R. Joshi^A. Khan^B. Knapmeyer-Endrun^J. Li^R. Maguire^W. T. Pike^H. Samuel^M. Schimmel^N. C. Schmerr^S. C. Stähler^E. Stutzmann^M. Wieczorek^Z. Xu^A. Batov^E. Bozdag^N. Dahmen^P. Davis^T. Gudkova^A. Horleston^Q. Huang^T. Kawamura^S. D. King^S. M. McLennan^F. Nimmo^M. Plasman^A. C. Plesal^E. Stepanova^E. Weidner^G. Zenhäusern^L. J. Daubar^B. Fernando^R. F. Garcia^L. V. Posiolova^M. P. Panning

Science, 378 (6618), • DOI: 10.1126/science.abq7157

An insightful impact

On 24 December 2021, the seismometer for the InSight mission on Mars detected a large seismic event with a distinct signature. Posiolova *et al.* discovered that the event was caused by a meteor impact on the surface of Mars, which was confirmed by satellite observations of a newly formed 150-kilometer crater. The surface nature and size of the impact allowed Kim *et al.* to detect surface waves from the event, which have yet to be observed on Mars. These surface waves help to untangle the structure of the Martian crust, which has various amounts of volcanic and sedimentary rock, along with subsurface ice, in different regions of the planet (see the Perspective by Yang and Chen). The characteristics of the impact itself are important because they provide a seismic fingerprint of an impact event that is different from the marsquakes observed so far. —BG

View the article online

<https://www.science.org/doi/10.1126/science.abq7157>

Permissions

<https://www.science.org/help/reprints-and-permissions>